RSC Advances

PAPER

View Article Online
View Journal | View Issue

Cite this: *RSC Adv.*, 2024, **14**, 37392

Highly flexible hybrid devices enabled by Ag-decorated $ZnCo_2O_4$ electrodes†

Xingjie Sun,[a] Wei-chao Zhang[b] and Xiang Wu *[a]

Electrode materials with excellent performance are the basis for designing supercapacitors with outstanding stability and high specific capacitance. In this work, we prepared a type of $ZnCo_2O_4$ nanosheet structure with Ag nanoparticles through a multi-step hydrothermal strategy. The as-fabricated composite presented a specific capacity of 2540 F g^{-1} at 1 A g^{-1} due to the synergetic effect of its components and structure. The three-dimensional structure enabled the material to maintain an initial specific capacitance of 92.5% after 10 000 cycles. The asymmetric supercapacitor delivered an energy density of 72.36 W h kg^{-1} at a power density of 10 800 W kg^{-1}. Moreover, it demonstrated 89% capacitance retention at 5 A g^{-1} after 10 000 cycles even when the operating temperature decreased to 0 °C.

Received 13th August 2024
Accepted 11th November 2024

DOI: 10.1039/d4ra05871b

rsc.li/rsc-advances

1. Introduction

The requirements for renewable and clean energy are increasing with the drive toward the sustainable development of human society.[1–3] At present, energy storage devices have been studied, including supercapacitors (SCs), fuel cells, and sodium-ion and lithium-ion batteries.[4–6] Among conventional rechargeable devices, SCs are one of the commonly used power sources for backup storage, portable electronic units and electric vehicles. They are generally divided into two categories: electrical double-layer capacitors (EDLCs) and pseudo-capacitors.[7,8] The EDLC energy-storage process is based on the potential difference between two solid electrodes,[9] whereas the pseudocapacitor energy-storage process involves a faradaic process that occurs at the surface of an electrode material. The latter is based on the use of electrochemical reactions adjacent and on the surface of the electrodes to achieve energy storage and involves reaction not only on the surface but also inside the entire electrode.[10–12] Consequently, it can achieve a higher specific capacity and energy density than EDLCs for the same electrode area. However, the low conductivity of the material hinders its large-scale application.[13–15] Therefore, research should focus on improving the rate capability, cycle life and capacity of SCs.

Transition metal oxides have attracted much attention as positive materials for SCs owing to their excellent theoretical capacity.[16,17] $ZnCo_2O_4$, possessing feasible oxidation states, presents a high electrochemical activity and reversible capacity. The synergistic effect between Zn and Co promotes electrical conductivity and mechanical stability.[18–20] Furthermore, the inverse spinel-structured $ZnCo_2O_4$ electrode can enable effective charge storage and provides ion channels. For example, urchin-like $ZnCo_2O_4$ materials revealed a specific capacity of 1841.8 F g^{-1} in 6 M KOH electrolyte.[21] The electrode demonstrated a capacity retention of about 78.4% at 10 A g^{-1} after 3000 cycles. However, such electrodes still encounter problems such as an unsatisfactory cycle life and slow ion diffusion at high multiplicities.[22–24] The volume of the electrode will change greatly in the charging–discharging process, which can lead to fragmentation of the active components and materials. The combination of $ZnCo_2O_4$ with other electrode materials has been a research hotspot to enhance electrochemical performances. Three-dimensional (3D) nanostructures offer a buffer for volume expansion.[25–27] Moreover, they can enhance the contact area between the electrolyte and the electrode material, thereby increasing active sites and improving electrochemical performances. Ag particles possess a large active surface area. For instance, Wang *et al.* prepared Ag nanoparticle-coated porous carbon materials with a specific capacity of 323.8 F g^{-1} at 0.5 A g^{-1}, which retained 93.2% of the initial special capacitance after 4000 cycles. The fabricated devices demonstrated an energy density of 15.9 W h kg^{-1} at 1120 W kg^{-1}.[28] Zhang *et al.* reported a $Au_{38-x}Ag_x$ NCs@ZIF-8 nanocomposite. The assembled capacitors achieved an energy density of 14.75 W h kg^{-1} at a power density of 2212.8 W kg^{-1}.[29]

Herein, we report Ag–$ZnCo_2O_4$ composites with a unique mesoporous structure. The sphere-like Ag-modified $ZnCo_2O_4$ nanosheets were fabricated by a hydrothermal strategy using nickel foam (NF) as the substrate. The as-prepared electrode delivered a specific capacity of 2540 F g^{-1} and retained 92.5% of

[a]School of Materials Science and Engineering, Shenyang University of Technology, Shenyang 110870, P. R. China. E-mail: wuxiang05@sut.edu.cn

[b]Key Laboratory of Engineering Dielectrics and Its Application, Ministry of Education, Harbin University of Science and Technology, Harbin 150080, P. R. China

† Electronic supplementary information (ESI) available. See DOI: https://doi.org/10.1039/d4ra05871b

the initial capacity at a current density of 10 A g^{-1} after 10 000 cycles. Moreover, the Ag–$ZnCo_2O_4$ product was used as a positive electrode to assemble several asymmetric SCs, which revealed a specific capacity of 253.33 F g^{-1} at 0.5 A g^{-1}. Also, 89% of the initial capacitances of Ag–$ZnCo_2O_4$//AC was retained after 10 000 cycles at 5 A g^{-1}, presenting an energy density of 72.36 W h kg^{-1} at a power density of 10 800 W kg^{-1}. The performances of the devices were also studied at 0 °C, and the result suggested that the capacitor lost only 33% of its initial specific capacitance.

2. Experimental

Sheet-like $ZnCo_2O_4$ samples were synthesized by adding ethylenediaminetetraacetic acid disodium (EDTA-2Na) with a strong blocking and chelating ability. Typically, 0.5821 g (2 mM) cobalt nitrate, 0.15 g (0.45 mM) EDTA-2Na, and 0.2975 g (1 mM) zinc nitrate were dissolved into 40 mL deionized (DI) water to form a homogeneous transparent solution. The above-mentioned solution and clean NF were kept at 160 °C for 12 h after stirring for 30 min. $AgNO_3$ powder was then added in various proportions (0, 0.05, 0.1, and 0.15 mM) to investigate the influence of Ag addition, and the as-fabricated samples were thus denoted as ZCO, 0.05Ag-ZCO, 0.1Ag-ZCO, and 0.15Ag-ZCO, respectively.

The anode in this experiment was mixed with activated carbon (AC), polyvinylidene fluoride, and carbon black as the raw materials according to a fixed ratio of 7 : 2 : 1. A small amount of *N*-methyl-2-pyrrolidone was then added to form a slurry. To prepare the electrolyte, 22 mL DI water was added into 2 g polyvinyl alcohol and stirred until the temperature reached 95 °C. Consequently, 5 mL of 3 M KOH solution was dissolved into the solution under the condition of 85 °C. The materials were soaked into the PVA-KOH electrolyte to evaporate the excess water before the device assembly. The devices were assembled by placing two electrodes facing each other in a sandwich structure. To balance the charges, the optimum mass ratio of the positive and negative electrodes was calculated according to the following formula:

$$q^- = q^+ \quad (1)$$

$$Q = C \times \Delta V \times m = I \times t \quad (2)$$

where t, I, ΔV, C, m and q represent the discharging time (s), current (A), working voltage window (V), specific capacitance (F g^{-1}), mass loading of electrode (g) and the amount of charge stored in the samples (C), respectively.

The pore-size distributions and N_2 adsorption–desorption isotherms of the as-prepared samples were characterized by the Brunauer–Emmett–Teller method (BET, JW-TB200). The phase and composition of the synthesized electrode materials were studied by X-ray photoelectron spectroscopy (XPS, Thermo Scientific; Kα) and X-ray diffraction (XRD, Bruker D8 ADVANCE; $\lambda = 0.1542$ nm, Cu Kα radiation, 40 kV). The microstructure and morphology of the samples were examined through scanning electron microscopy (SEM, HiRes). The low-temperature electrochemical performance was estimated using an incubator (Neware). Hg/HgO rod was utilized as the counter electrode, Pt foil as the reference one and the 0.1Ag-ZCO sample as the working one. The electrochemical performance of the as-obtained electrode was evaluated in an electrochemical workstation (Shanghai Chenhua, CHI660E). A three-electrode system was utilized to perform the galvanostatic charge–discharge (GCD), electrochemical impedance spectroscopy (EIS) and cyclic voltammetry (CV) measurements.

3. Results and discussion

Fig. 1(a) shows the XRD patterns of ZCO, and the 0.05Ag-ZCO, 0.1Ag-ZCO, and 0.15Ag-ZCO composites. Sharp characteristic peaks could be observed at 18.96°, 31.22°, 36.81°, 39.49°, 48.99°, 55.57°, 59.28°, 65.15°, and 68.53°, which were indexed to the (111), (220), (311), (111), (222), (331), (511), (440), and (531) crystal planes of the ZCO electrodes, respectively (JCPDS No.23-1390). Moreover, two diffraction peaks were observed at 69.1° and 66.38° in the as-prepared material, suggesting the presence of ZnO (JCPDS No.36-1451). Furthermore, the peaks located at 38.12°, 44.28°, 64.43°, and 77.47° could be ascribed to the (111), (200), (220), and (311) planes (JCPDS No. 04-0785). It could thus be clearly seen that material well match the typical crystal of Ag, indicating that Ag was successfully incorporated in the Ag–$ZnCo_2O_4$ electrode. There were also several evident peaks of the Ni element (PDF card No. 87-0712), which came from the Ni substrate.

XPS was used to investigate the surface states and surface chemical composition of the as-fabricated 0.1Ag-ZCO hierarchical structures. Fig. 1(b) shows the fitting spectra. The binding energies at 1019.84, 778.7, 527.7, 365.3, and 280.4 eV were in accordance with Zn 2p, Co 2p, Ag 3d, O 1s, and C 1s, respectively. The high-resolution spectrum of Ag 3d possessed two main peaks at binding energies of 367.02 and 373.07 eV, belonging to Ag $3d_{5/2}$ and Ag $3d_{3/2}$, respectively, indicating the existence of free Ag (Fig. 1(c)).[30] The XPS O 1s spectrum in S1(a)† presented peaks for lattice oxygen (O_{lat}), adsorbed oxygen (O_{ads}), and molecular water (H_2O) at binding energies of 530, 531.28, and 532.06 eV.[31] As displayed in Fig. 1(d), the spectrum of Co 2p was composed of two spin orbital Co $2p_{3/2}$ and Co $2p_{1/2}$ characteristic peaks, respectively, located at binding energies of 794.69 and 779.27 eV. The fitting spectrum of the sample revealed that the characteristic peaks at 782.13/797.3 and 779.27/794.69 eV belonged to Co^{2+} and Co^{3+}, respectively.[32] In Fig. 1(e), the Zn 2p spectrum was split into peaks at 1043.52 (Zn $2p_{3/2}$) and 1020.38 eV (Zn $2p_{1/2}$).[33]

The N_2 adsorption–desorption isotherm curves were plotted used to study the specific surface area and pore-size distribution of the as-obtained composites. As shown in Fig. 1(f) and S1(b) and S1(c),† the hysteresis loops and isotherm types of the samples demonstrated type H3 and IV curves, respectively, manifesting that all the electrodes possessed a mesoporous structure and the adsorption and desorption process was almost completely reversible.[34] The as-fabricated 0.1Ag-ZCO compound presented a larger specific surface area (39.7 m^2 g^{-1}) than the ZCO (13.9 m^2 g^{-1}), 0.05Ag-ZCO (35.2 m^2 g^{-1}), and

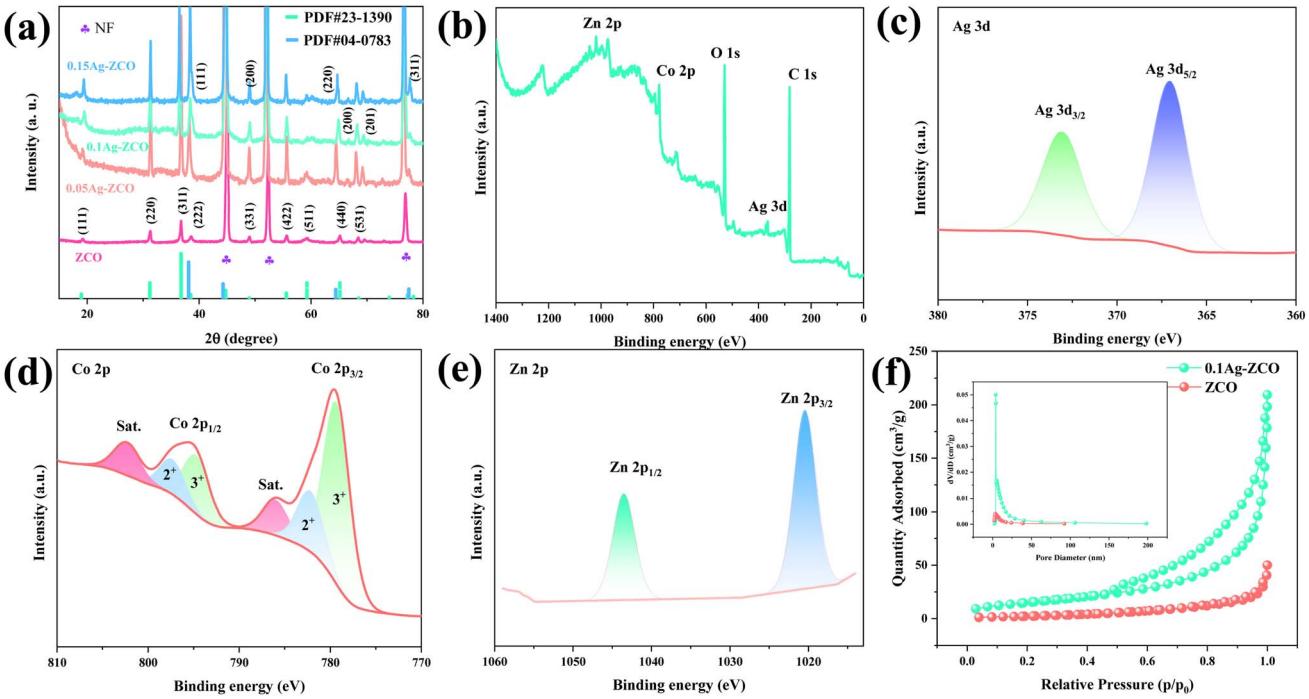

Fig. 1 Structure characterization of the as-prepared materials. (a) XRD patterns of the electrode materials, (b) XPS full spectrum of ZCSN-2, (c–e) XPS spectra of Ag 3d Co 2p and 2 Zn p and (f) N_2 adsorption–desorption isotherms and corresponding pore-size distribution curves (inset) of ZCO and 0.01Ag-ZCO.

0.15Ag-ZCO (25.6 m^2 g^{-1}) materials. The inset reveals similar the pore-size distributions of the ZCO and 0.1Ag-ZCO samples. The pore size was mostly less than 10 nm and decreased rapidly with the increasing diameter due to their identical surface structure.[35] Therefore, the pore size and distribution of the 0.1Ag-ZCO composite were conducive to ion/charge accumulation and forming an adequate electrode–electrolyte interface.

Next, we investigated the morphology and microstructure of the as-synthesized materials through SEM. The ZCO electrode presented a smooth sheet-like structure, with a 165 nm average thickness (Fig. 2a and e). According to Fig. 2b and f, Ag nanoparticle uniformly grew on the surface of the ZCO nanosheet. SEM images of the 0.1Ag-ZCO materials are shown in Fig. 2c and g, indicating the formation of a 3D core–shell structure. The morphology of the sample demonstrated a certain agglomeration state, which may have been due to the presence of EDTA-2Na reagent during the synthesis. EDTA-2Na contains two pairs of electrons and four carboxyl functional groups on the nitrogen atom. It is typically used as a binding site, giving EDTA-2Na a strong chelation and blocking ability. The morphology of the sample presents certain agglomeration state. This may be due to the presence of EDTA-2Na reagent during synthesis. EDTA-2Na contains two pairs of electrons and four carboxyl functional groups on the nitrogen atom. It is used as a binding site, inducing EDTA-2Na blocking ability and strong chelation. Similar findings have been reported for $BiPO_4$ nanoparticles in the previous literature.[36] With the increase in Ag content, the nucleation rate of the particles was higher than the growth rate, which is unfavorable for control of the morphology (Fig. 2d and h). Fig. 2(i–l) show the EDS pattern and different color mapping images of the ZCO and 0.1Ag-ZCO materials, respectively, showing that Ag, Co, Zn, and O elements were evenly distributed. The above findings allowed concluding that Ag nanoparticles had been successfully composited with ZCO in the samples, and due to the introduction of silver, the conductivity of the samples was improved while maintaining the richness of the pores of the electrode material.

To confirm the effect of the Ag element, we evaluated the electrochemical performances of the as-obtained composites. Fig. 3(a) shows the CV curves of ZCO, 0.05Ag-ZCO, 0.1Ag-ZCO, and 0.15Ag-ZCO at 10 mV s^{-1}. The distinct oxidation and reduction peaks indicated that the electrodes possessed typical pseudocapacitive behaviors. The closed curves area of the 0.1Ag-ZCO sample was larger than those of the other electrode materials under the same condition. The reversible faradaic reaction was the main reason for the appearance of the redox activity, as described in eqn (3)–(5):[37–39]

$$ZnCo_2O_4 + OH^- + H_2O \leftrightarrow ZnOOH + 2CoOOH + e^- \quad (3)$$

$$CoOOH + OH^- \leftrightarrow CoO_2 + H_2O + e^- \quad (4)$$

$$2Ag + 2OH^- \leftrightarrow Ag_2O + H_2O + 2e^- \quad (5)$$

The discharging time of the 0.1Ag-ZCO sample (1270 s) was longer than those of ZCO (397 s), 0.05Ag-ZCO (895 s), and 0.15Ag-ZCO (1085 s) electrodes under the same experimental conditions. The specific capacities were 794, 1790, 2540, and

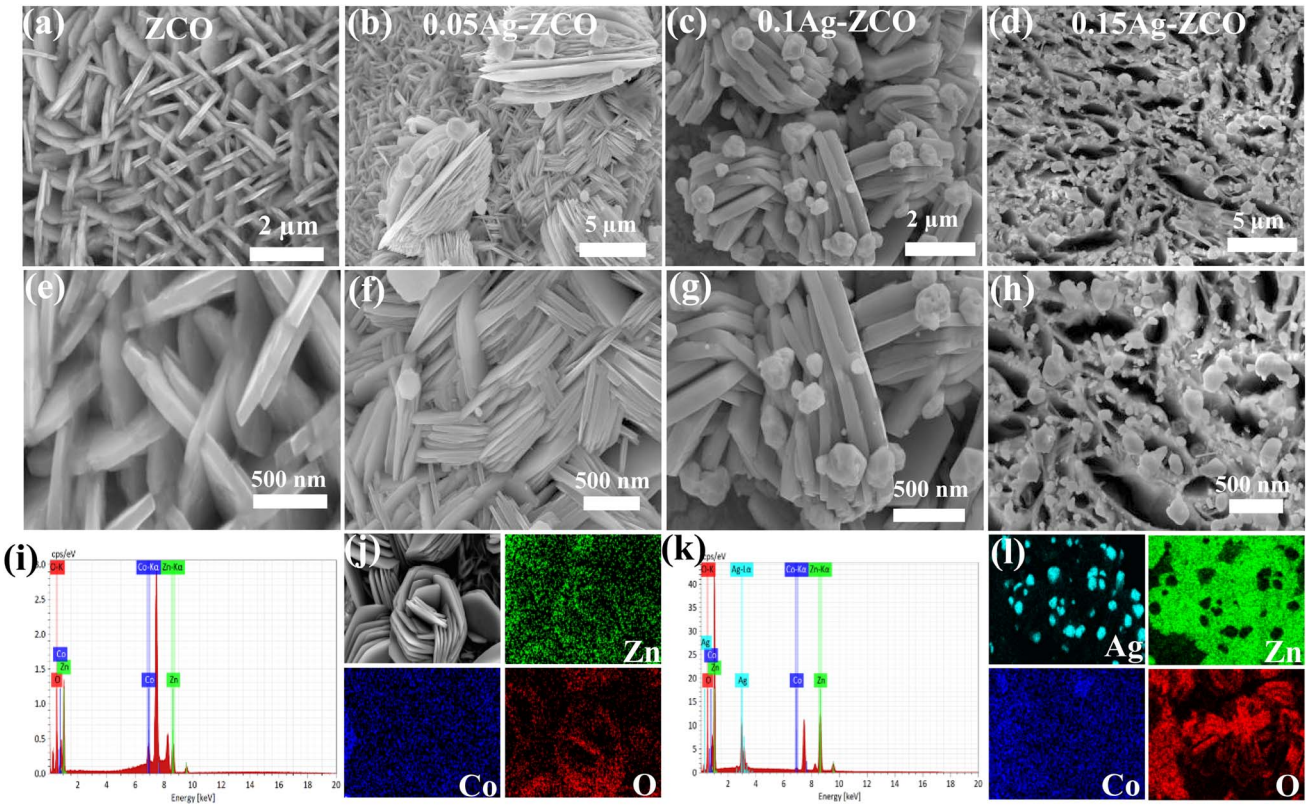

Fig. 2 Morphology of the samples. SEM images of (a and e) ZCO, (b and f) 0.05Ag-ZCO, (c and g) 0.05Ag-ZCO, (d and h) 0.05Ag-ZCO. (i–l) EDS pattern and elemental mapping images of the ZCO and 0.05Ag-ZCO samples.

2170 F g^{-1} at 1 A g^{-1}, respectively (Fig. 3(b)). These results prove that the composite material improved the specific capacity and electrochemical performance of the electrode material. In addition, Fig. 3(c) illustrates the CV curves of the 0.1Ag-ZCO electrode at different scanning rates. The peak current increased dramatically as the scan rate increased from 10 to 100 mV s^{-1}, indicating a rapid redox reaction. The structure of the as-prepared electrodes demonstrated a considerably enhanced specific surface area while the addition of silver enhanced the conductivity, facilitating the diffusion of electrons and ions because of the small resistance between the active substances.[40] This resulted in the formation of an excellent conductive network within the electrode. Moreover, the polarization phenomenon occurred with the increase in the scan rate.[41] The potentials of the oxidation and reduction peaks were shifted positively and negatively, respectively. Fig. 3(d) shows the GCD curves of the 0.1Ag-ZCO sample at various current densities. The values of C were calculated from the discharging curves and eqn (2), as shown in Fig. 3(e). The sample delivered specific capacities of 2540, 2230, 1920, 1680, and 1500 F g^{-1} at current densities of 1, 2, 4, 6, and 10 A g^{-1}, respectively. This suggests a large number of electrolyte ions will be adsorbed in a short time when the current increases, which will cause the concentration at the interface between the electrode and the electrolyte to drop rapidly, also slowing down the diffusion rate and the polarization.[42] As the applied voltage continues to increase, the rate of charge growth after the formation of the control step will remain relatively slow. Therefore, the capacity of the electrodes will decrease under high-current conditions. Fig. S2† illustrates the CV and GCD curves of the ZCO, 0.05Ag-ZCO, 0.15Ag-ZCO samples. A comparison of the as-prepared 0.1A-ZCO samples with other reported materials is provided in Table 1.[43–47]

The electrical conductivity and reaction kinetics of the as-fabricated electrodes were evaluated through EIS plots (Fig. 3(f)) at frequencies from 10 mHz to 100 Hz. The Nyquist curve of the electrode consists of two parts: the diagonal line and an arc at the low- and high-frequency parts, respectively. The intersection of the curves with the real axis of impedance gives the internal resistance (R_s), and the values for the tested samples here were 0.49, 0.43, 0.45 and 0.43 Ω. The line reflects the Warburg impedance caused by the diffusion of cations between the interface electrolyte and the electrode. The curve of the 0.1Ag-ZCO sample was approximately perpendicular to the axis, presenting a clear capacitive reactance characteristic, which indicates that most of the capacitance can be efficiently utilized. The diameter of the semicircle refers to the charge-transfer resistance (R_{ct}). A low interfacial R_{ct} indicates outstanding kinetics of the electrode's faradaic reaction.[48] This is favorable for high-current discharging performance and the specific capacity. Consider the following equation:

$$Z = \sigma_w \omega^{-1/2} + R_{ct} + R_s, \quad (6)$$

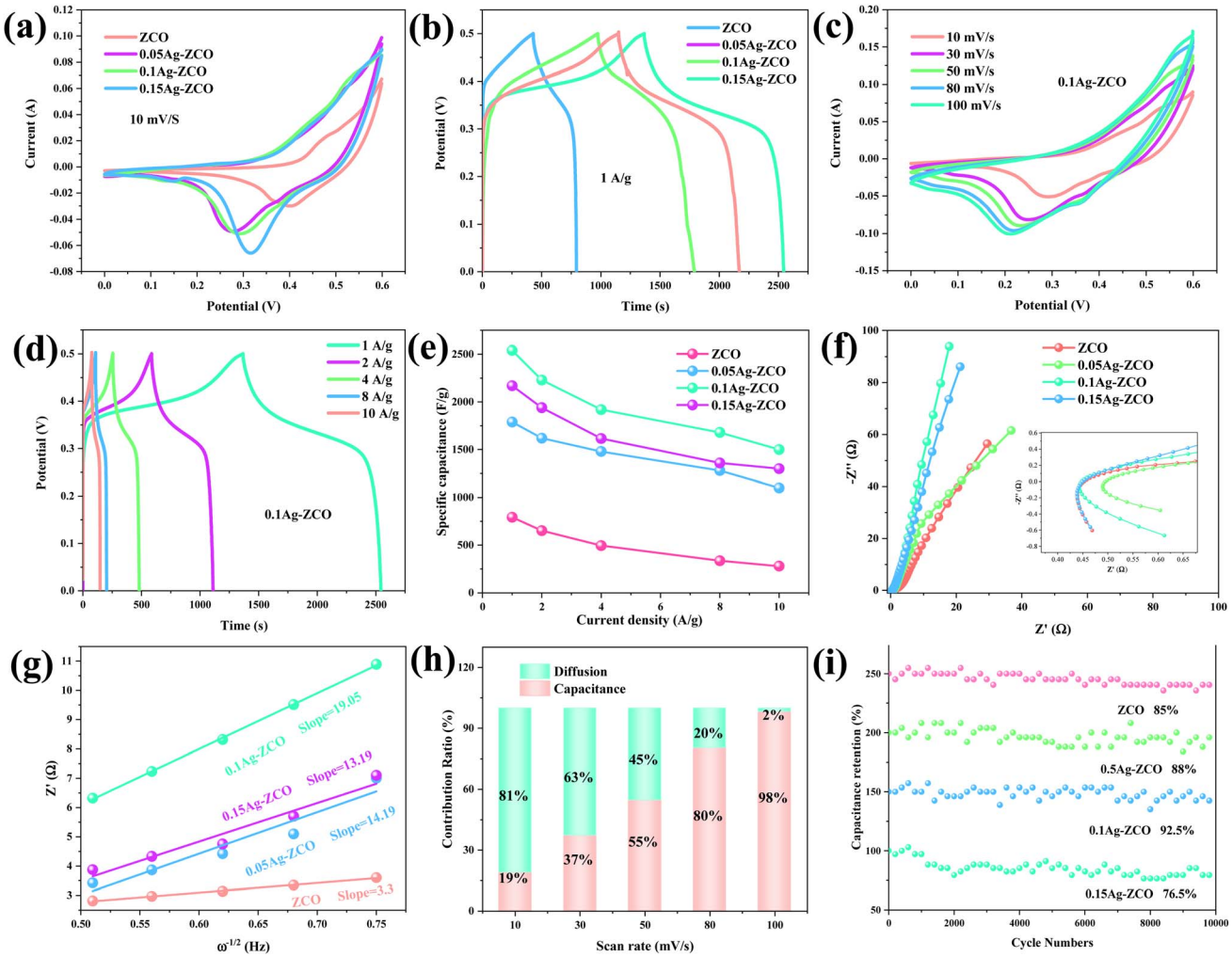

Fig. 3 Electrochemical performances. (a) CV curves at 10 mV s^{-1}. (b) GCD curves at a current density of 1 A g^{-1}. (c) CV curves of 0.1Ag-ZCO samples at different scan rates. (d) GCD curves of 0.1Ag-ZCO samples at different current densities. (e) Comparison of the specific capacity at various current densities, (f) Nyquist plots. (g) Z' as a function of $\omega^{-1/2}$. (h) Contribution ratio between the surface-controlled and diffusion-limited capacities, and (i) cycling performance at 10 A g^{-1}.

Table 1 Electrochemical performance of several electrode materials

Materials	Capacitance	Current density	Electrolyte	Ref.
$ZnCo_2O_4$	662.4 F g^{-1}	2 A g^{-1}	2 M KOH	43
$NiMoO_4$–Ag/rGO	1132.8 F g^{-1}	1 A g^{-1}	6 M KOH	44
N-O_v-$ZnCo_2O_4$@CC	2166.4 F g^{-1}	1 A g^{-1}	6 M KOH + 0.2 M Zn-acetate	45
$(CoOH)_2$/Ag	729 F g^{-1}	0.5 A g^{-1}	3 M KCl	46
$ZnCo_2O_4$ MFs-20/20	746.4 F g^{-1}	1 A g^{-1}	2 M KOH	47
0.1Ag-ZCO	2540 F g^{-1}	1 A g^{-1}	3 M KOH	This work

where Z, σ_w, R_{ct}, ω, and R_s are the diffusive resistance, Warburg factor, transmission resistance, angular frequency and internal resistance, respectively. In Fig. 3(g), the slopes of all the electrodes were 3.3, 14.19, 19.05, and 13.9, showing that the composites possessed a high kinetic behavior for electrochemical reactions because of the rapid OH^- transfer.

The percentage contributions of the diffusion-controlled ($k_2v^{1/2}$) and capacitive-controlled processes (k_1v) were studied quantitatively. From Fig. 3(h), the contribution ratio between the surface and diffusion-limited capacities of the 0.1Ag-ZCO sample increased from 18% to 98% in the range of 10–100 mV s^{-1}. The as-prepared electrode demonstrated surface-control capacitance, suggesting a high charge-transfer efficiency. This result is related to its preeminent electrical conductivity, improved band gap width, and abundant active sites. As a supercapacitor material, its charging–discharging

efficiency directly affects the cost and service life of the SC. Fig. 3(i) indicates that the initial capacitance loss of the 0.1Ag-ZCO samples was only 7.5%, which was less than the 15%, 12%, and 23.5% losses in the other samples.

Several capacitors were fabricated using the as-synthesized 0.1Ag-ZCO material as a cathode and AC as an anode. Fig. 4(a) presents the CV curves of the two electrodes within the potential ranges of −1 to 0 V and 0–0.6 V at 100 mV s^{-1}, respectively. The AC and 0.1Ag-ZCO electrodes presented electrical double-layer capacitance and faradaic pseudocapacitance energy storage mechanisms, respectively. From Fig. 4(b), the CV curve of 0.1Ag-ZCO//AC at different scan rates (10–100 mV s^{-1}) basically maintained the same shape without obvious distortion, demonstrating the fast reversible property of the device. The specific capacities of 0.1Ag-ZCO//AC were calculated to be 253.33, 208, 172.53, 128.64, 119.47, and 106.67 F g^{-1} at 0.5, 1, 2, 4, 8, and 10 A g^{-1}, respectively, and its charging–discharging time could reach 874.1 s at 0.5 A g^{-1} (Fig. 4(c)). The CV curves of the assembled devices were studied in various potential windows at 100 mV s^{-1}, as shown in Fig. 4(d). The shapes changed due to the decomposition of the electrolyte when the voltage was increased to 1.8 V. This indicate that the ASC could stably work up to 1.7 V only.

Electrochemical performance tests were also conducted at different bending angles to further explore the application of the assembled ASC in flexible wearable electronic devices. Fig. S3† shows digital images of a folded device. The integral area of the curve did not change, indicating that there was no obvious capacity decay after folding (Fig. 4(e)). Fig. 4(f) shows the GCD curves of the device at different bending degrees from 0° to 180°. Only a small fluctuation was found with the change in bending angle, indicating only a small loss of capacitance. EIS was next utilized to evaluate the electronic and ionic conductivity and thus estimate the electrochemical dynamics processes. The capacitors demonstrated R_s values of 1.46 Ω, as described in the inset in Fig. 4(g). After the device was bent, the folded R_s value was smaller than the initial one, probably because the folding made the electrode surface contact more

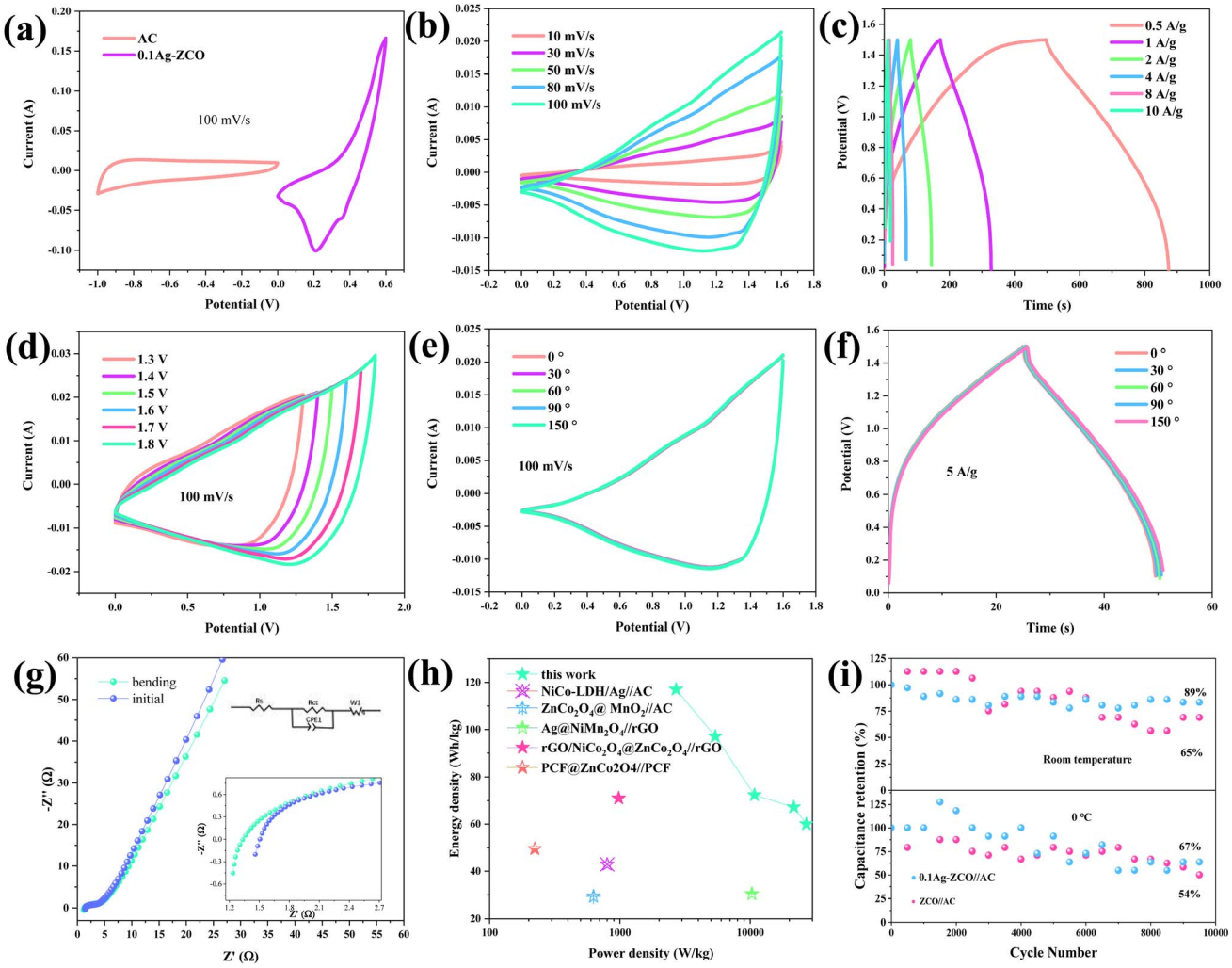

Fig. 4 Electrochemical performance of the ASC device. (a) CV curves of the electrodes at 100 mV s^{-1}, (b) CV curves at various scan rates, (c) GCD curves at various current densities, (d) CV curves in different potential windows at 100 mV s^{-1}, and CV (e) and GCD (f) curves at various bending angles, (g) Nyquist plots, (h) Ragone plots, and (i) cycling performance at 5 A g^{-1}.

fully with the electrolyte. The observed increase in R_{ct} after folding was related to the inevitable shedding of the active material during the folding process, resulting in a slight increase in resistance. Moreover, with the increase in the diffusion impedance in the low-frequency region, a charge transfer tendency appeared on the surface of the active material. This may be due to the increased contact interface between the gel electrolyte and the active material and the greater charges migration to the surface of the electrode material.

The following equations can be used to obtain the corresponding power density (P) and energy density (E):

$$E = 1/2Cv^2 \quad (7)$$

$$P = 3600E/\Delta t \quad (8)$$

From Fig. 4(h), the ASC presented an energy density of 117 W h kg^{-1} at 2700 W kg^{-1}. It could also maintain 60 W h kg^{-1} at 27 000 W kg^{-1} even at a high current density of 10 A g^{-1}. The 0.1Ag-ZCO electrode possessed the largest energy density than other reported works, such as NiCo-LDH/Ag//AC (42.9 W h kg^{-1} at 800 W kg^{-1}), rGO/$NiCo_2O_4$@$ZnCo_2O_4$//rGO (71 W h kg^{-1} at 980 W kg^{-1}), PCF@$ZnCo_2O_4$//PCF (49.5 W h kg^{-1} at 222.7 W kg^{-1}), Ag@$NiMn_2O_4$//rGO (30.44 W h kg^{-1} at 10 300.6 W kg^{-1}), and $ZnCo_2O_4$@MnO_2//AC (29.41 W h kg^{-1} at 628.4 W kg^{-1}).[49–53] The initial specific capacitance of the device was maintained at 89% at room temperature after 10 000 charging/discharging cycles. The device demonstrated a 33% energy loss under the same experimental conditions when the temperature was further reduced to 0 °C. The assembled ZCO//AC using the same method could retain 65% and 54% of the initial capacity at room temperature and 0 °C, respectively, indicating that the materials had excellent low-temperature electrochemical stability (Fig. 4(i)). The compatibility between the electrolyte with the electrode and the diaphragm became worse at low temperature; whereby the conductivity of the device decreased and R_{ct} increased significantly. Fig. S4† shows that the 0.1Ag-ZCO material retained its original morphology after multiple charging–discharging processes.

4. Conclusions

In summary, a straightforward two-step hydrothermal route was used to fabricate a unique 3D porous structural 0.1Ag-ZCO composite, which was then applied as an electrode material for a supercapacitor and demonstrating good stability and high electrochemical activity. The special micro-architecture enhanced the cycling stability of the as-fabricated samples. Moreover, the addition of Ag element greatly reduced the intrinsic conductivity, accelerated charge transfer and ion diffusion and exposed abundant active sites. The mechanical stability and rate capacity of the nanostructure were obviously enhanced compared with the ZCO sample. The excellent performance was attributed to the adhesion between Ag particles and the substrate. The assembled capacitors revealed outstanding flexible mechanical and low-temperature electrochemical stability.

Data availability

Data will be made available on request.

Author contributions

Xingjie Sun: methodology, conceptualization, software, data curation, writing – original draft preparation. Xiang Wu and Wei-chao Zhang: supervision, writing – reviewing and editing.

Conflicts of interest

The authors declare that they have no known competing financial interests or personal relationships that could have appeared to influence the work reported in this paper.

Acknowledgements

This project is supported by National Natural Science Foundation of China (No. 52172218) and Key Laboratory of Engineering Dielectrics and Its Application (Harbin University of Science and Technology), Ministry of Education (KFM202309).

References

1 A. Sumboja, J. Liu, W. G. Zheng, Y. Zong, H. Zhang and Z. Liu, *Chem. Soc. Rev.*, 2018, **47**, 5919–5945.
2 Y. Liu and X. Wu, *J. Energy Chem.*, 2023, **87**, 334–341.
3 Y. Liu, Y. Liu, X. Wu and Y. R. Cho, *ACS Appl. Mater. Interfaces*, 2022, **149**, 11654–11662.
4 H. N. Abdelhamid, S. A. A. Kiey and W. Sharmoukh, *Appl. Organomet. Chem.*, 2022, **361**, e6486.
5 S. Acharya, S. De and G. C. Nayak, *ACS Appl. Electron. Mater.*, 2023, **51**, 406–417.
6 A. Agarwal and B. R. Sankapal, *Dalton Trans.*, 2022, **51**, 13878–13891.
7 Y. C. Sun, X. W. Wang, A. Umar and X. Wu, *RSC Adv.*, 2022, **12**, 14858–14864.
8 M. Dai, D. Zhao, H. Liu, X. Zhu, X. Wu and B. Wang, *ACS Appl. Energy Mater.*, 2021, **43**, 2637–2643.
9 L. Han, J. Li, X. Zhang, H. Huang, Z. Yang, G. Zhu, M. Xu and L. Pan, *ACS Sustainable Chem. Eng.*, 2021, **928**, 9165–9176.
10 X. Huai, J. Liu and X. Wu, *Chin. J. Struct. Chem.*, 2023, **42**, 100158.
11 K. Zhang, X. Gao, F. Yao, Y. Q. Xie, H. Bai, Y. J. Sun, R. Liu and H. Y. Yue, *J. Colloid Interface Sci.*, 2023, **650**, 105–111.
12 Y. T. Li, C. R. Zhao, A. Abdukader and X. Wu, *RSC Adv.*, 2024, **14**, 9594–9601.
13 H. Liu, M. Dai, D. Zhao, X. Wu and B. Wang, *ACS Appl. Energy Mater.*, 2020, **37**, 7004–7010.
14 J. Liu, S. Zhao, A. Umar and X. Wu, *Mater. Today Sustain.*, 2023, **23**, 100433.
15 X. Sun, D. Zhang, A. Umar and X. Wu, *ACS Appl. Energy Mater.*, 2023, **618**, 9594–9601.
16 J. Liu, S. Zhao and X. Wu, *Chin. Chem. Lett.*, 2024, **357**, 109059.

17 A. Meftahi, A. R. Vanani and M. Shabani-Nooshabadi, *Fuel*, 2023, **331**, 125683.
18 M. M. Mohamed, M. Khairy, A. A. Amer and M. A. Mousa, *J. Mater. Res. Technol.*, 2022, **21**, 2555–2570.
19 X. Wang, Y. Sun, W. C. Zhang and X. Wu, *Chin. Chem. Lett.*, 2023, **343**, 107593.
20 J. Zhang and X. Wu, *Int. J. Miner. Metall. Mater.*, 2024, **311**, 179–185.
21 C. Wu, J. J. Cai, Q. B. Zhang, X. Zhou, Y. Zhu, L. J. Li, P. K. Shen and K. L. Zhang, *Electrochim. Acta*, 2015, **169**, 202–209.
22 S. Yu, Y. Ye, M. Yang, Y. Liu, D. Yang, H. Li and B. Liu, *Small*, 2024, **208**, 306267.
23 J. Zhang, X. Wu and S. Luo, *Batteries Supercaps*, 2024, **77**, e202400205.
24 K. Zhang, J. Jia, L. Tan, S. Qi, B. Li, J. Chen, J. Li, Y. Lou and Y. Guo, *J. Power Sources*, 2023, **577**, 233239.
25 D. Zhao, M. Dai, H. Liu, Z. Duan, X. Tan and X. Wu, *J. Energy Chem.*, 2022, **69**, 292–300.
26 L. Zhao, H. Guo, Y. Li, Z. Liu and R. Song, *Nanoscale*, 2024, **164**, 1880–1889.
27 S. Zhao, J. Liu and X. Wu, *Ionics*, 2023, **29**, 5267–5273.
28 R. Wang, X. Li, Z. Nie, Q. Jing, Y. Zhao, H. Song and H. Wang, *J. Energy Storage*, 2022, **51**, 104364.
29 M. Shoeb, M. Mobin, S. M. Adnan, I. I. Ansari, M. N. Khan, S. Zaidi and M. Y. Ansari, *Surface. Interfac.*, 2022, **28**, 101650.
30 R. Yuan, J. Wang, X. Luo, G. Wang, D. Wang, S. Liu and Z. Zhao, *Energy Fuels*, 2023, **382**, 1496–1507.
31 X. Hu, C. Wan, X. Meng, A. Tang and X. Ju, *Appl. Surf. Sci.*, 2022, **582**, 152456.
32 S. Hunpratub, T. Chullaphan, S. Chumpolkulwong, N. Chanlek and S. Phokha, *Mater. Chem. Phys.*, 2023, **303**, 127820.
33 J. Hur, B. Hwang, L. Hong, S. J. Yoo and S. E. Chun, *Surface. Interfac.*, 2023, **40**, 103127.
34 J. Li, J. Li, M. Shao, Y. Yan and R. Li, *Nanomaterials*, 2023, **137**, 1229.
35 M. Li, B. Xu, L. Zheng, J. Zhou, Z. Luo, W. Li, W. Ma, Q. Mao, H. Xiang and M. Zhu, *Carbon*, 2023, **203**, 455–461.
36 S. Vadivel, D. Maruthamani, M. Kumaravel, B. Saravanakumar, B. Paul, S. S. Dhar, K. Saravanakumard and V. Muthuraj, *J. Taibah Univ. Sci.*, 2017, **11**, 661–666.
37 D. Nayak and R. B. Choudhary, *J. Mater. Sci.*, 2023, **58**, 9160–9180.
38 S. Nayak, A. A. Kittur and S. Nayak, *Chem. Phys. Lett.*, 2022, **806**, 140058.
39 S. Nee Lou, M. Choon Heng See, S. Lim, N. Sharma, J. Scott, D. W. Wang, R. Amal and Y. Hau Ng, *ChemSusChem*, 2021, **14**, 2882–2891.
40 H. Reddy Inta, S. Vishwanathan, H. S. S. R. Matte, S. Ghosh, A. Roy and V. Mahalingam, *Chemelectrochem*, 2023, **102**, 201041.
41 S. Vishwanathan and H. S. S. R. Matte, *Chem. Commun.*, 2023, **59**, 9263–9266.
42 M. Yan, B. Yang, X. Sun, Z. Wang, X. Jiang, W. Yi, H. Sun, R. Yang, H. Ding, D. Yue, K. Zhai, Y. Li, X. Chen, Y. Zhang and X. Liu, *ACS Mater. Lett.*, 2023, **61**, 194–202.
43 H. Y. Sun, Y. Miao, G. J. Wang, X. X. Han, Y. L. Wang, Z. Y. Zhang, C. W. Luo, X. H. Liu, C. J. Xu and H. Y. Chen, *J. Energy Storage*, 2023, **72**, 108502.
44 B. Huang, D. Yao, J. Yuan, Y. Tao, Y. Yin, G. He and H. Chen, *J. Colloid Interface Sci.*, 2022, **606**, 1652–1661.
45 X. Zhang, M. S. Javed, S. S. A. Shah, F. Ahmed, I. Hussain, F. M. Alzahrani, N. S. Alsaiari, S. M. Eldin, M. Z. Ansari and W. Han, *Electrochim. Acta*, 2023, **461**, 142654.
46 M. He, W. Xu, Y. Wu, Z. Dong and L. Lv, *Inorg. Chem. Commun.*, 2019, **104**, 150–154.
47 H. Y. Sun, Y. Miao, G. J. Wang, X. L. Ren, E. H. Bao, X. X. Han, Y. L. Wang, X. Y. Ma, C. J. Xu and H. Y. Chen, *J. Energy Storage*, 2024, **76**, 109780.
48 W. Yang, L. Hou, P. Wang, Y. Li, R. Li, B. Jiang, F. Yang and Y. Li, *Green Energy Environ.*, 2022, **74**, 723–733.
49 T. Guan, L. Fang, L. Liu, F. Wu, Y. Lu, H. Luo, J. Hu, B. Hu and M. Zhou, *J. Alloys Compd.*, 2019, **799**, 521–528.
50 A. J. C. Mary, C. I. Sathish, A. Vinu and A. C. Bose, *Energy Fuels*, 2020, **348**, 10131–10141.
51 H. Niu, X. Yang, H. Jiang, D. Zhou, X. Li, T. Zhang, J. Liu, Q. Wang and F. Qu, *J. Mater. Chem. A*, 2015, **347**, 24082–24094.
52 M. I. A. A. Maksoud, M. A. M. Elsaid and M. A. Elkodous, *J. Energy Storage*, 2022, **56**, 105938.
53 D. Yu, Z. Zhang, Y. N. Meng, Y. Teng, Y. Wu, X. Zhang, Q. Sun, W. Tong, X. Zhao and X. Liu, *Inorg. Chem. Front.*, 2018, **53**, 597–604.